Check for updates

Helvetica Chimica Acta

HELVETICA chimica acta

RESEARCH ARTICLE OPEN ACCESS

Mechanosynthesis of Metal-Free Molecular Perovskites

Gianluca Bravetti[1] | Aki Frankberg[2] | Mahsa Shahsavan[2] | Paul Zimmermann[3] | Benjamin M. Gallant[4] | Oleg Konovalov[5] | Mohammad Reza Golobostanfard[2] | Alexander Hinderhofer[3] | Frank Schreiber[3] | Dominik J. Kubicki[4] | Jovana V. Milić[1,2]

[1]Adolphe Merkle Institute, University of Fribourg, Fribourg, Switzerland | [2]Department of Chemistry, University of Turku, Turku, Finland | [3]Institut Für Angewandte Physik, University of Tübingen, Tübingen, Germany | [4]Department of Chemistry, University of Birmingham, Birmingham, UK | [5]European Synchrotron Radiation Facility (ESRF), The European Synchrotron, Grenoble, France

Correspondence: Dominik J. Kubicki (d.j.kubicki@bham.ac.uk) | Jovana V. Milić (jovana.milic@unifr.ch)

Received: 22 December 2025 | **Revised:** 10 April 2026 | **Accepted:** 28 April 2026

Keywords: ball milling | DABCO-based perovskites | metal-free halide perovskites | molecular perovskites | water-assisted mechanosynthesis

ABSTRACT

Metal-free halide perovskites have recently emerged as promising candidates for optoelectronic applications. However, their synthesis has largely depended on water-based single-crystal growth that limits material diversity, scalability, and practical implementation. Here, we present a mechanochemical route to synthesize *N,N*-diazabicyclo[2.2.2]octonium (H-DABCO)-based halide perovskites from the $(DABCO)(NH_4)X_3$ (X = I, Br) compositions. The structural properties were confirmed by X-ray diffraction and solid-state nuclear magnetic resonance spectroscopy. Thin films were prepared from mechanosynthetic powders by spin-coating and characterized by in-situ grazing incidence wide-angle scattering measurements, as well as by UV–vis absorption and steady-state photoluminescence spectroscopy. This mechanosynthetic strategy provides a scalable, environmentally friendly pathway to broaden the scope of metal-free perovskites and advance their potential in sustainable optoelectronic technologies.

1 | Introduction

Halide perovskite semiconductors have revolutionized the field of optoelectronics over the past decade owing to their exceptional optoelectronic properties [1–3]. However, conventional halide perovskites typically contain toxic metals and exhibit environmental instability that limits their practical application [4–6]. These challenges have driven interest in more sustainable alternative materials. In this context, metal-free molecular perovskites (MOPs) have recently emerged as promising candidates [7–9]. They adopt the general ABX_3 perovskite structure, in which the A sites are occupied by divalent organic cations, B sites by ammonium cations, and X represents halide anions, such as iodide or bromide (Figure 1). MOPs have already demonstrated remarkable ferroelectric properties, including high spontaneous polarization and elevated phase-transition temperatures, surpassing those of conventional inorganic ferroelectrics, such as $BaTiO_3$ [9]. These features make them attractive for use in emerging memory devices, sensors, and energy harvesting technologies [4, 10, 11]. Despite this promise, the synthesis of MOPs has relied primarily on slow evaporation methods to grow single crystals from aqueous solutions at elevated temperatures [7, 9, 12]. While suitable for fundamental investigations, these techniques face significant challenges for large-scale production and material diversification. Moreover, solubility limitations of certain organic cations restrict the accessible material space, and the meticulous control required for crystal growth hinders industrial scalability [13]. Given these practical limitations, mechanochemical synthesis offers a promising alternative. This solvent-free approach induces chemical reactions through mechanical force, such as grinding

Gianluca Bravetti, Aki Frankberg, and Mahsa Shahsavan contributed equally to this work.

Dedicated to the Presidents of the Bürgenstock Conferences 2024 (Prof. Erick Carreira) and 2025 (Prof. Jose Luis Mascareñas).

This is an open access article under the terms of the Creative Commons Attribution-NonCommercial License, which permits use, distribution and reproduction in any medium, provided the original work is properly cited and is not used for commercial purposes.
© 2026 The Author(s). *Helvetica Chimica Acta* published by Wiley-VHCA AG.

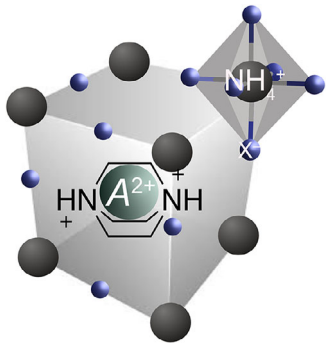

FIGURE 1 | Schematic representation of the metal-free perovskite (ABX_3) structure with *N,N*-diazabicyclo[2.2.2]octonium (H-DABCO)-based central (A) cations (green spheres), NH_4^+ cations as B sites (grey spheres), and halide (X = I, Br) anions (purple spheres).

solid reactants [14–16]. It has been successfully employed to prepare metal halide perovskites and other functional materials, offering advantages such as improved sustainability, scalability, and access to compounds that are poorly soluble in conventional solvents [17–19]. However, its application to MOPs remains largely unexplored [10, 20].

Herein, we report the mechanochemical synthesis of *N,N*-diazabicyclo[2.2.2]octonium (H-DABCO)-based metal-free halide perovskites, specifically based on (H-DABCO)$(NH_4)I_3$ and (H-DABCO)$(NH_4)Br_3$ compositions, by using ball milling. We find that water-assisted ball milling facilitated the formation of the desired molecular perovskite phases, which were confirmed by X-ray diffraction (XRD) and solid-state nuclear magnetic resonance (ssNMR) spectroscopy. Subsequently, thin films were fabricated from mechanosynthetic powders via spin-coating, and their structural properties were investigated by in situ grazing incidence wide-angle X-ray scattering (GIWAXS) to evidence the formation of the perovskite phase. Finally, optical properties were assessed to evaluate their suitability for optoelectronic applications. Our findings demonstrate that solvent-free or solvent-assisted mechanochemistry provides a suitable and sustainable route to metal-free (H-DABCO)-based halide perovskites, thereby enabling greater material diversity and future integration into functional devices.

2 | Results and Discussion

We have performed mechanochemical synthesis of the (H-DABCO)$(NH_4)I_3$ and (H-DABCO)$(NH_4)Br_3$ MOPs by ball milling stoichiometric amounts of the corresponding precursors, namely (H-DABCO)X_2 and NH_4X (X = I, Br; the methodology is detailed in the Experimental Section). This involved various milling conditions (i.e., milling duration and media) and annealing treatments, whereas the resulting powders were investigated by a combination of characterization techniques. The structures of the resulting powders were analyzed by XRD and compared with the corresponding single-crystal data of (H-DABCO)$(NH_4)I_3$ and (H-DABCO)$(NH_4)Br_3$, which were synthesized following the previously reported procedures [8]. After 30 min of ball milling (25 Hz) at ambient temperature, the XRD patterns of the resulting powders revealed diffractions that differed from those of the starting materials, indicating that the applied mechanical energy was sufficient to drive the reaction under ambient conditions (Figures S1 and S2). To advance the reaction without altering the milling conditions, a solvent-assisted mechanochemical approach was employed by adding a small amount of deionized water (up to 10 μL per 200 mg of powder) to the mixture to promote ionic rearrangements during perovskite phase formation [14, 16]. After 15 min of water-assisted mechanosynthesis, the XRD patterns of the resulting powders displayed new signals, such as at 22.7° and 26° for (H-DABCO)$(NH_4)Br_3$, which were consistent with the formation of the halide perovskite phase (Figure 2) [8]. The XRD patterns of the mechanosynthesized powders closely matched those of the calculated patterns derived from the corresponding single-crystal data [8], confirming the formation of the metal-free halide perovskite phases (Figures S1 and S2). We further investigated the impact of annealing temperatures by heating at 80°C and 100°C, which had a minor effect on the resulting structure, likely due to the removal of minor defects and residual precursors from the powder materials (as shown in Figure S3 and Table S1). We have thereby relied on water-mediated mechanosynthesis conditions to prepare the resulting powders without further optimization.

Atomic-level structures of (H-DABCO)$(NH_4)I_3$ and (H-DABCO)$(NH_4)Br_3$ perovskites were further investigated using magic angle spinning (MAS) ssNMR spectroscopy (Figures 3 and S4). In the ^{1}H NMR spectra, the perovskites displayed features consistent with –CH– and –NH– protons of $(H\text{-}DABCO)^{2+}$ and NH_4^+ (Figure S4). Some deviations were observed, including signals in (H-DABCO)I_2 suggestive of partial single protonation $(H\text{-}DABCO)^+$, and additional narrow peaks in (H-DABCO)Br_2 likely arising from solvent residues (Figure S4). In contrast, the ^{1}H-^{13}C cross-polarization (CP) NMR spectra showed distinct chemical shift changes relative to the H-DABCO-based precursors that provide evidence for the incorporation of $(H\text{-}DABCO)^{2+}$ into the environment of the halide perovskite frameworks (Figure 3). The observed signal broadening can be attributed to differences in crystallinity and static disorder, with narrower signals for the bromide analog (Figure 3, left) compared to the iodide (Figure 3, right). The changes in the structure, such as hydrogen bonding in the resulting material, were also apparent by Fourier-transformed infrared spectroscopy (FTIR; Figure S5).

Having confirmed the formation of the perovskite structure in the mechanosynthesized powders, they were used to prepare thin films by spin-coating after dissolving them in dimethyl sulfoxide (DMSO) on glass substrates (in accordance with the procedure detailed in the Experimental Section). The process was monitored in situ using GIWAXS to track perovskite formation (Figure 4). Before the spin-coating process, we observed several peaks in the thin-film solution, consistent with the trigonal (H-DABCO)$(NH_4)Br_3$ structure and the precursor structure in the mechanosynthesized powders (Figure 2). This indicates that nanoparticles obtained by mechanosynthesis remain in solution during the film fabrication process. When spin-coating began, peaks from the trigonal and precursor structures intensified, and an intermediate phase (q = 0.59 Å^{-1}) appeared (Figure 4a–d). As peaks from the intermediate structure disappeared during solvent evaporation, this is likely due to intercalated solvent molecules. Upon annealing, this intermediate structure and the

15222675, 0, Downloaded from https://onlinelibrary.wiley.com/doi/10.1002/hlca.202500237 by Universitatsbibliothek, Wiley Online Library on [03/07/2026]. See the Terms and Conditions (https://onlinelibrary.wiley.com/terms-and-conditions) on Wiley Online Library for rules of use; OA articles are governed by the applicable Creative Commons License

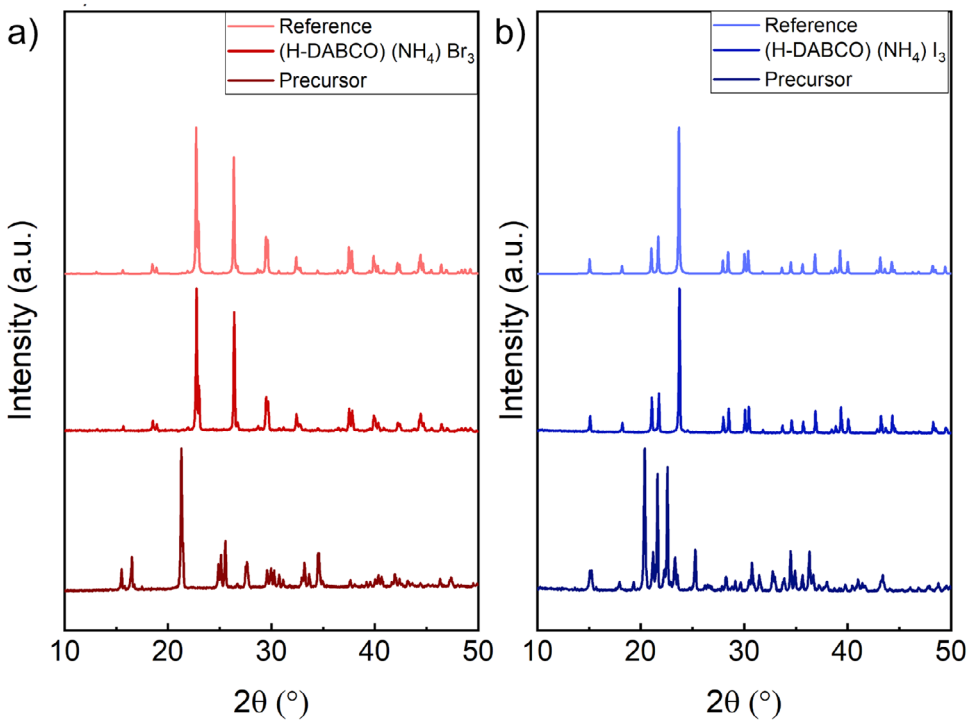

FIGURE 2 | Structural properties of (H-DABCO)(NH_4)X_3 mechanosynthesized powders based on x-ray diffraction. XRD patterns for (a) bromide (X = Br) and (b) iodide (X = I) compositions compared with the (H-DABCO)X_2 precursors and crystal structure reference systems (CCDC: 1836336 and 1836327 from ref [8]). Further comparison of the ball milling conditions (including different milling durations, media, and annealing temperatures) resulted in comparable XRD patterns, with changes associated mainly with the crystallite size, as shown in Figures S1–S3 and Table S1.

trigonal (H-DABCO)(NH_4)Br_3 phase converted completely to the cubic phase, which was indicated by the disappearance of the intermediate peak (at 0.59 $Å^{-1}$; Figure 4a) and the (210) peak of the trigonal phase (Figure 4d). After annealing, the GIWAXS data showed peaks attributable only to the cubic (H-DABCO)(NH_4)Br_3 structure, with lattice parameters consistent with the single-crystal structure (Figure S6) [8], and to the precursor structure observed in the powder. Both exhibited randomly oriented domains (Figure S6); however, the diffraction rings exhibited markedly different substructures (Figure S7). Specifically, the diffraction rings from the precursor phase were continuous, suggesting a relatively small domain size. In contrast, the diffraction rings from the cubic structure were non-continuous with bright signals originating from larger domains. The radial widths of the diffraction rings slightly decreased during the annealing process, which indicates grain growth from the remaining precursor for both the precursor and the cubic phase. Notably, the larger precursor grains convert to a more uniform phase, with smaller grains formed between spin-coating and subsequent annealing. The precursor can be fully converted to the perovskite phase in thin films by annealing the films at 120°C (Figure S8). Finally, measurements of the resulting films at room temperature reveal that (H-DABCO)(NH_4)Br_3 remains in the cubic perovskite phase (Figure S6), indicating the formation and stability of H-DABCO-based metal-free perovskites under the thin-film preparation conditions. Scanning electron microscopy (SEM) images revealed large crystallites on the surface of thin films (Figure S9), suggesting the need for optimization of film formation to achieve compact film morphologies. Having evidenced their formation and assessed their morphology, we further investigated optical properties.

The optical properties of thin films were examined by UV–vis absorption and steady-state photoluminescence (PL) spectroscopy (Figure 5). The absorption spectra of the H-DABCO-based perovskites exhibited edges near 300 and 350 nm (Figure S10), consistent with their wide bandgaps for related systems [12, 21–23]. The corresponding optical transition energies were estimated at 3.1–3.2 eV for iodide- and 3.2–3.4 eV for bromide-based compositions based on the absorption onsets and the emission spectra (Figures 5 and S10, detailed in the Experimental section). The lower energies compared to reported values (above 4) eV likely reflect optically active transitions associated with excitonic or localized states rather than the bandgap. While the nature of the bandgap has been studied theoretically [24], further investigation is required to fully understand the opto-electronic characteristics of this emerging class of metal-free molecular perovskites. Nonetheless, the successful fabrication of mechanosynthesized powders and thin films highlights the potential of these materials for future applications that remain to be exploited.

3 | Conclusions

In conclusion, we have developed a mechanochemical method for synthesizing H-DABCO–based metal-free halide perovskite materials. The introduction of a small amount of water proved beneficial for the formation of the resulting crystalline phases, as evidenced by XRD, ssNMR spectroscopy, and in situ GIWAXS measurements. The fabrication of thin films and their optical characterization demonstrates the potential for optoelectronic applications, which require further investigation. This work

15222675, 0, Downloaded from https://onlinelibrary.wiley.com/doi/10.1002/hlca.202500237 by Universitatsbibliothek, Wiley Online Library on [03/07/2026]. See the Terms and Conditions (https://onlinelibrary.wiley.com/terms-and-conditions) on Wiley Online Library for rules of use; OA articles are governed by the applicable Creative Commons License

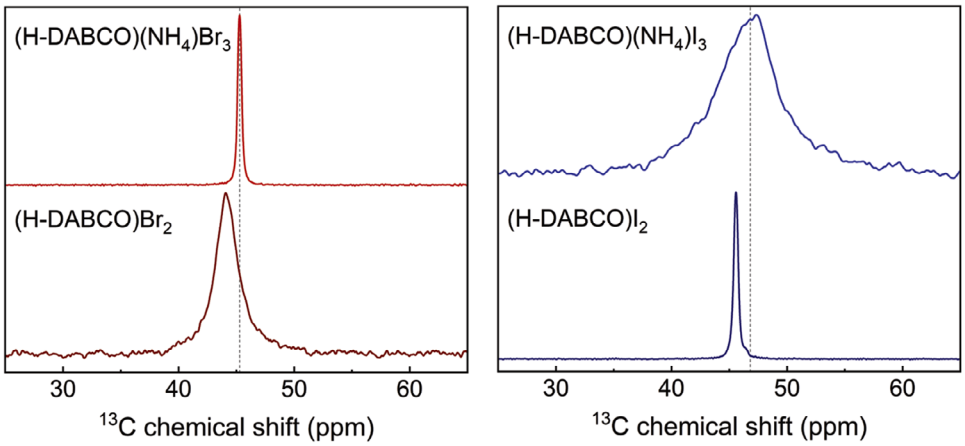

FIGURE 3 | Structural properties of (H-DABCO)(NH_4)X_3 mechanosynthesized powders based on solid-state NMR spectroscopy. ^{1}H-^{13}C CP ssNMR spectra recorded with 20 kHz MAS at 298 K for the (H-DABCO)X_2 precursors (X = Br, I) and mechanosynthesized (H-DABCO)(NH_4)Br_3 (left) and (right) (H-DABCO)(NH_4)I_3 perovskite powders. Complementary ^{1}H NMR data are shown in Figure S4.

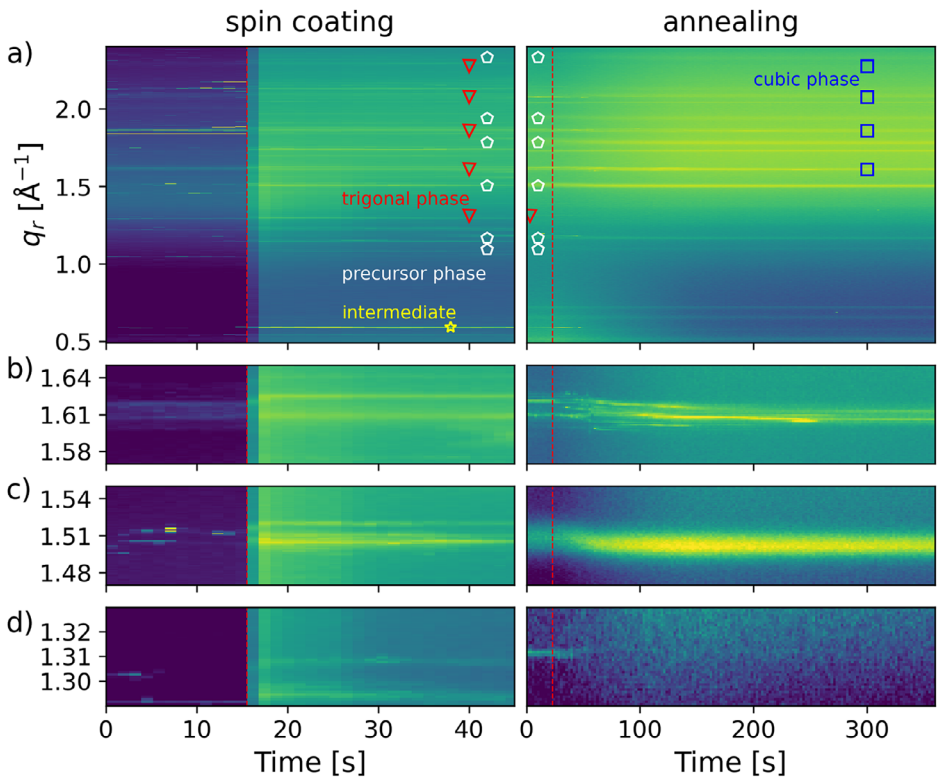

FIGURE 4 | Structural properties of (H-DABCO)(NH_4)X_3 thin films. Intensity maps from radial profiles of in-situ GIWAXS measurements for the spin-coating process (left) and the annealing process (right). Vertical lines mark the start of spin-coating and annealing in the respective images. Intensity maps from radial profiles of GIWAXS measurements in (a) shows the complete *q*-range with marked peaks, (b) at first the (202) and (006) peak for the *trigonal* (H-DABCO)(NH_4)Br_3 phase and after the conversion the (111) peak for the *cubic* phase, (c) the dominant peak for the *precursor* peak, and (d) the (210) peak for the *trigonal* phase.

represents an important step toward scalable and sustainable production of metal-free perovskites by using mechanosynthesis as a viable alternative to traditional solution-based methods, thereby advancing the development of sustainable materials and broadening opportunities for their applications. Ongoing research focuses on the ferroelectric properties of these materials, their operational stability, and integration into functional devices for energy technologies.

4 | Experimental Section

All chemicals were used without further purification. *N,N*-Diazabicyclo[2.2.2]octane (DABCO, Sigma-Aldrich, ≥99%), hydriodic acid (HI, 57 wt% in water, Sigma-Aldrich), hydrobromic acid (HBr, 48 wt% in water, Sigma-Aldrich), ammonium iodide (NH_4I, Sigma-Aldrich, ≥99%), ammonium bromide (NH_4Br, Sigma-Aldrich, ≥99%), diethyl ether (Sigma-Aldrich, ≥99.5%),

15222675, 0, Downloaded from https://onlinelibrary.wiley.com/doi/10.1002/hlca.202500237 by Universitatsbibliothek, Wiley Online Library on [03/07/2026]. See the Terms and Conditions (https://onlinelibrary.wiley.com/terms-and-conditions) on Wiley Online Library for rules of use; OA articles are governed by the applicable Creative Commons License

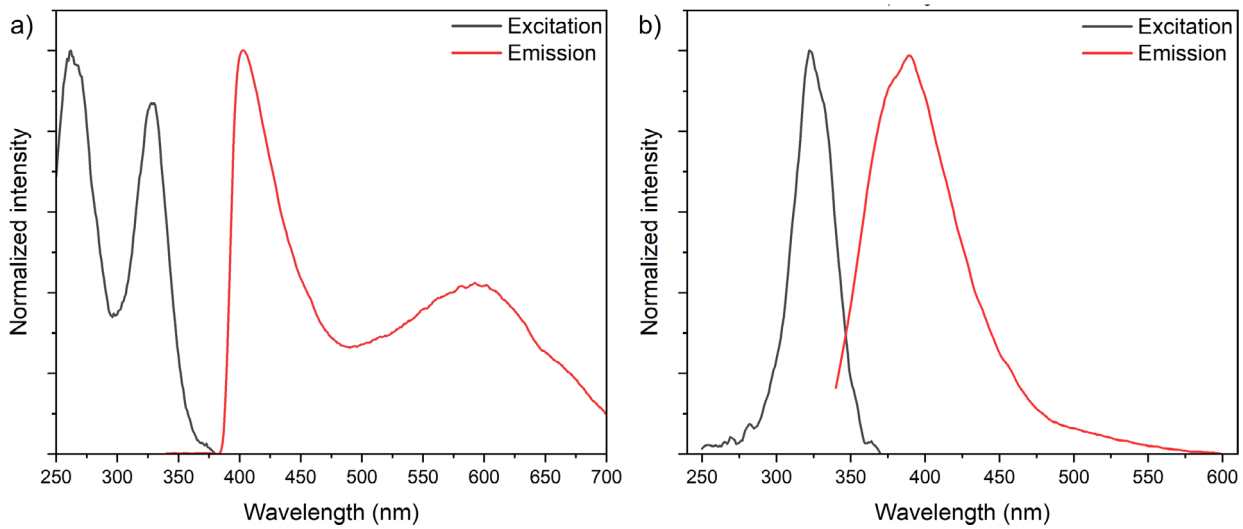

FIGURE 5 | Optical properties of (H-DABCO)(NH_4)X_3 perovskite thin films. Photoluminescence excitation (black) and emission (red) spectra of (a) iodide (X = I) and (b) bromide (X = Br) compositions on microscope glass slides. Optical transition energies were estimated from the excitation (and UV–vis absorption) onsets and PL emission maxima. Complementary UV–vis absorption spectra for the bandgap estimates are shown in Figure S10.

and dimethyl sulfoxide (DMSO, Sigma-Aldrich, ≥99.9%) were used in the material synthesis.

H-DABCO spacer cation synthesis was based on the protonation of the precursor. *H-DABCO iodide (H-DABCO-I) and bromide (H-DABCO-Br)* were prepared by protonating DABCO with the respective hydrohalic acids, following reported methods in the literature [7, 8]. DABCO (0.01 mol, 1.12 g) was dissolved in 20 mL of deionized water, and an equimolar amount of HI or HBr was added dropwise under stirring at room temperature. The reaction mixture was stirred for 1 h to ensure complete protonation. The solvent was then evaporated under reduced pressure to yield the corresponding halide salts as white crystalline solids, which were dried in a vacuum oven at 40°C overnight.

Single crystals were grown following the method of Ye et al. to serve as structural references [8]. *(H-DABCO)(NH_4)I_3*: (H-DABCO)I_2 (0.2 g) and NH_4I (0.1 g) were dissolved in 10 mL of deionized water under gentle heating at 50 °C to form a clear solution. The solution was filtered to remove undissolved particles, then cooled slowly to room temperature. The solution was left undisturbed at ambient conditions for several days, during which colorless crystals formed. The crystals were collected by filtration, washed with cold deionized water, and dried in air. *(H-DABCO)(NH_4)Br_3*: A similar procedure was followed using (H-DABCO)Br_2 (0.2 g) and NH_4Br (0.1 g). The components were dissolved in 10 mL of deionized water under gentle heating to obtain a clear solution. Slow cooling and evaporation over several days yielded colorless crystals, which were collected and dried in air under ambient conditions.

Mechanochemical reactions were conducted using a Retsch MM400 ball mill equipped with a Teflon holder that accommodated plastic Eppendorf tubes. Glass (2 mm diameter) or steel (4 mm diameter) beads were used as grinding media to enable efficient mixing (without any observable impact of the grinding material type). *(H-DABCO)(NH_4)Br_3*: (H-DABCO)Br_2 (73.70 mg) and NH_4Br (26.70 mg) were weighed and placed in a 2 mL Eppendorf tube, along with a 4 mm steel ball, as the milling medium. The tube was secured in a Teflon holder and milled at 25 Hz. The resulting powder was transferred to a glass vial and annealed at 80°C for 30 min in a vacuum oven, affording a grey powder (94% yield). For the water-assisted method, 10 µL of deionized water was added to the mixture before milling to facilitate the process under the same conditions. *(H-DABCO)(NH_4)I_3*: (H-DABCO)I_2 (71.70 mg) and NH_4I (28.20 mg) were mixed and ball-milled under the same conditions as the bromide derivative. The product was a bright white powder (95.8 % yield). For the water-assisted method, 10 µL of deionized water was added to the mixture prior to milling to facilitate grinding under the same conditions.

Thin-film fabrication was based on spin-coating the solutions onto the prepared glass substrates. *Glass substrates* were cleaned thoroughly before film deposition. They were first scrubbed with a 2% Hellmanex solution using a brush and then sonicated in the same solution for 10 min. After rinsing with deionized water and ethanol to remove detergent residues, the substrates were sonicated in acetone for 10 min, rinsed with isopropanol, and sonicated again in isopropanol for 10 min. Finally, the substrates were dried under a nitrogen stream and plasma-cleaned for 10 min to enhance surface wettability and remove residual organics. *Spin-coating* of halide perovskite powders was performed using solutions in DMSO at concentrations up to 0.2 M, heated to approximately 80 °C to facilitate dissolution. The solutions were cooled to room temperature and filtered through a 0.45 µm PTFE syringe filter. Spin-coating was performed in a nitrogen-filled glovebox to prevent exposure to moisture. An aliquot of the filtered solution was dispensed onto the cleaned substrate, and spin-coating was performed by accelerating to 1000 rpm at 500 rpm s^{-1} and holding for 10 s before 2000 rpm for 30 s to yield a uniform film. The films were then annealed at 120°C for 10 min on a hotplate to promote solvent evaporation and crystallization.

Characterization was based on the following techniques. *X-ray diffraction (XRD) measurements* were conducted using a

15222675, 0, Downloaded from https://onlinelibrary.wiley.com/doi/10.1002/hlca.202500237 by Universitatsbibliothek, Wiley Online Library on [03/07/2026]. See the Terms and Conditions (https://onlinelibrary.wiley.com/terms-and-conditions) on Wiley Online Library for rules of use; OA articles are governed by the applicable Creative Commons License

Panalytical Aeris diffractometer with Cu Kα 1 and 2 radiations (λ = 1.540 and 1.544 Å) in the 2θ range of 5° to 80°. The step size was 0.022°, and the scan rate was 0.91 per step. XRD patterns were used to analyze the crystalline phases and assess the purity of the synthesized materials. *Scanning electron microscopy (SEM)* was performed using a field emission SEM (FEI Nova NanoSEM 450) to examine the morphology and surface topology of the thin films. *FTIR spectra* recorded with a Fourier-transform infrared spectroscopy (FT-IR) with a Vertex 70 device with a diamond probe ATR setup, DTGS detector. 64 scans were performed, and all data were recorded in transmittance mode with a resolution of 4 cm^{-1}. In the setup, the sample is pressed against a diamond anvil. *UV–vis absorption spectroscopy* was performed with an Agilent Cary 60 integrating sphere by measuring reflectance in a powder holder with a quartz-glass window. Scan ranges from 500 to 200 nm, with a scanning rate of 600 nm/min. Background determination was done by measuring 100%T off the $BaSO_4$ sample to the target UV-zone and 0%T by blocking the beam path. Reflectance was calculated into absorbance by applying Kubelka–Munk function $F(R) = \frac{(1-R)^2}{2R}$. This was plotted versus photon energy (hv) for the Tauc plot, and to estimate the bandgap of the resulting system (previously reported to be >4 eV) [12, 21–23]. *Photoluminescence (PL) spectroscopy* was conducted using a Horiba Fluorolog spectrometer. Steady-state PL spectra were recorded at room temperature with an excitation corresponding to the absorption of each material. *Solid-state NMR spectroscopy* was performed on a Bruker Avance Neo 20 T spectrometer equipped with a 4 mm MAS probe. ^{13}C spectra (213.79 MHz) were recorded at room temperature using cross-polarization at 12 kHz MAS with 100 kHz SPINAL-64 ^1H decoupling. *GIWAXS measurements* were performed on the ID10 beamline (at the ESRF; beam energy 22.5 keV, beam size 95 µm × 95 µm, Eiger4M detector at distances of 0.683 m). Real-time measurements were performed at an incidence angle equal to 0.5° in a nitrogen atmosphere. For in-situ measurements, halide perovskite powders were dissolved in a solvent mixture of DMF and DMSO with a volume ratio of 1:1 to obtain solutions with a concentration of 0.2 M. The solution-processed films were fabricated by spin coating. The precursor solution was deposited on the glass substrate and spun at 1000 and 4000 rpm for 10 s and 20 s, respectively. The spin-coated films were annealed with a halogen lamp at a target temperature for 10 min.

Author Contributions

The research was conceptualized by J.V.M. and primarily conducted by G.B. (preliminary work) and A.F. (complementary synthesis optimization and analysis). They prepared the first manuscript draft with the support of M.S., who also performed complementary structural analysis. NMR study was performed by B.G. and D.J.K., and GIWAXS analysis by P.Z., with the support of A.H., O.K., and F.S., while M.R.G. supported the analysis of optical properties and the revision of the manuscript. All authors contributed to the manuscript and discussion.

Acknowledgments

G.B. and J.V.M. are grateful to the Swiss National Science Foundation (SPARK project no. 221017) for supporting the early early work on this project. The authors received funding from the European Research Council Horizon programme for innovation under the grant agreement no. 101114653 (project "SmartHyMat"), and they acknowledge the European Synchrotron Radiation Facility (ESRF) for providing synchrotron radiation facilities under proposal number SC-5693, ID10 beamline, as well as the support of Ivan Zaluzhnyy and Niels Scheffczyk during the Beamtime. We also thank the BMBF for supporting project 05K19VTA (ERUM-PRO). The authors appreciate Prof. Loreta Muscarella and Dr. Susan A. Rigter (VU Amsterdam, The Netherlands) for collaborative exchanges and discussions on the topic of metal-free halide perovskites.

Open access publishing facilitated by Turun yliopisto, as part of the Wiley - FinELib agreement.

Conflicts of Interest

The authors declare no conflicts of interest.

Data Availability Statement

Data presented here can be accessed at the DOI:10.5281/zenodo.20282438, and it is available under the license CC-BY-4.0 (Creative Commons Attribution-ShareAlike 4.0 International). GIWAXS data measured at the ESRF is available at DOI:10.15151/ESRF-ES-2113933332.

References

1. B. Saparov and D. B. Mitzi, "Organic–Inorganic Perovskites: Structural Versatility for Functional Materials Design," *Chemical Reviews* 116 (2016): 4558–4596, https://doi.org/10.1021/acs.chemrev.5b00715.

2. "A Century of Ferroelectricity," *Nature Materials* 19 (2020):129, https://doi.org/10.1038/s41563-020-0611-1.

3. G. Sharada, P. Mahale, B. P. Kore, et al., "Is $CH_3NH_3PbI_3$ Polar?," *Journal of Physical Chemistry Letters* 7 (2016): 2412–2419.

4. S. Horiuchi and Y. Tokura, "Organic Ferroelectrics," *Nature Materials* 7 (2008): 357–366, https://doi.org/10.1038/nmat2137.

5. L. W. Martin and A. M. Rappe, "Thin-Film Ferroelectric Materials and Their Applications," *Nature Reviews Materials* 2 (2016): 16087, https://doi.org/10.1038/natrevmats.2016.87.

6. S. Shkuratov and C. Lynch, "A Review of Ferroelectric Materials for High Power Devices," *Journal of Materiomics* 8 (2022): 739–752.

7. X. Song, G. Hodes, K. Zhao, and S. (Frank) Liu, "Metal-Free Organic Halide Perovskite: A New Class for Next Optoelectronic Generation Devices," *Advanced Energy Materials* 11 (2021): 2003331, https://doi.org/10.1002/aenm.202003331.

8. H.-Y. Ye, Y.-Y. Tang, P.-F. Li, et al., "Metal-Free Three-dimensional Perovskite Ferroelectrics," *Science* 361 (2018): 151–155, https://doi.org/10.1126/science.aas9330.

9. W. Li and L.-J. Ji, "Perovskite Ferroelectrics Go Metal Free," *Science* 361 (2018): 132, https://doi.org/10.1126/science.aat5729.

10. L. A. Muscarella, G. Bravetti, and J. V. Milić, "The Emergence of Metal-Free Molecular Perovskites: Challenges and Opportunities," *Materials Horizons* 12 (2025): 6124–6132, https://doi.org/10.1039/D4MH01877J.

11. H.-Y. Liu, H.-Y. Zhang, X.-G. Chen, and R.-G. Xiong, "Molecular Design Principles for Ferroelectrics: Ferroelectrochemistry," *Journal of the American Chemical Society* 142 (2020): 15205–15218, https://doi.org/10.1021/jacs.0c07055.

12. X. Song, Q. Cui, Y. Liu, et al., "Metal-Free Halide Perovskite Single Crystals With Very Long Charge Lifetimes for Efficient X-Ray Imaging," *Advanced Materials* 32 (2020): 2003353, https://doi.org/10.1002/adma.202003353.

13. M. A. Green, A. Ho-Baillie, and H. J. Snaith, "The Emergence of Perovskite Solar Cells," *Nature Photonics* 8 (2014): 506–514, https://doi.org/10.1038/nphoton.2014.134.

14. T. Friščić, C. Mottillo, and H. M. Titi, "Mechanochemistry for Synthesis," *Angewandte Chemie International Edition* 59 (2020): 1018–1029.

15222675, 0, Downloaded from https://onlinelibrary.wiley.com/doi/10.1002/hlca.202500237 by Universitatsbibliothek, Wiley Online Library on [03/07/2026]. See the Terms and Conditions (https://onlinelibrary.wiley.com/terms-and-conditions) on Wiley Online Library for rules of use; OA articles are governed by the applicable Creative Commons License

15. J.-L. Do and T. Friščić, "Mechanochemistry: A Force of Synthesis," *ACS Central Science* 3 (2017): 13–19, https://doi.org/10.1021/acscentsci.6b00277.

16. S. L. James, C. J. Adams, C. Bolm, et al., "Mechanochemistry: Opportunities for New and Cleaner Synthesis," *Chemical Society Reviews* 41 (2011): 413–447, https://doi.org/10.1039/C1CS15171A.

17. F. Palazon, Y. El Ajjouri, and H. J. Bolink, "Making by Grinding: Mechanochemistry Boosts the Development of Halide Perovskites and Other Multinary Metal Halides," *Advanced Energy Materials* 48 (2019): 1902499.

18. S. Pagola, "Outstanding Advantages, Current Drawbacks, and Significant Recent Developments in Mechanochemistry: A Perspective View," *Crystals* 13 (2023): 124, https://doi.org/10.3390/cryst13010124.

19. M. Solares-Briones, G. Coyote-Dotor, J. C. Páez-Franco, et al., "Mechanochemistry: A Green Approach in the Preparation of Pharmaceutical Cocrystals," *Pharmaceutics* 13 (2021): 790, https://doi.org/10.3390/pharmaceutics13060790.

20. F. Lyu, Z. Chen, R. Shi, J. Yu, and B.-L. Lin, "Solid Phase Synthesis of Metal-free Perovskite Crystalline Materials," *Journal of Solid State Chemistry* 304 (2021): 122548, https://doi.org/10.1016/j.jssc.2021.122548.

21. X. Liu, Q. Cui, H. Li, et al., "Biocompatible Metal-Free Perovskite Membranes for Wearable X-Ray Detectors," *ACS Applied Materials & Interfaces* 16 (2024): 16300–16308, https://doi.org/10.1021/acsami.4c01069.

22. Q. Cui, X. Liu, N. Li, et al., "A New Metal-Free Molecular Perovskite-Related Single Crystal With Quantum Wire Structure for High-Performance X-Ray Detection," *Small* 20 (2024): 2308945, https://doi.org/10.1002/smll.202308945.

23. H. Li, T. Li, C. Ma, et al., ""One-Click Restart" Recycling of Metal-Free Perovskite X-Ray Detectors," *Advanced Materials* 36 (2024): 2400783, https://doi.org/10.1002/adma.202400783.

24. J. Bie, D.-B. Yang, M.-G. Ju, et al., "Molecular Design of Three-Dimensional Metal-Free $A(NH_4)X_3$ Perovskites for Photovoltaic Applications," *JACS Au* 1 (2021): 475–483, https://doi.org/10.1021/jacsau.1c00014.

Supporting Information

Additional supporting information can be found online in the Supporting Information section.

Additional structural and optoelectronic information is provided in the Supporting Information.

Supporting File 1: hlca70077-sup-0001-SuppMat.pdf.

15222675, 0, Downloaded from https://onlinelibrary.wiley.com/doi/10.1002/hlca.202500237 by Universitatsbibliothek, Wiley Online Library on [03/07/2026]. See the Terms and Conditions (https://onlinelibrary.wiley.com/terms-and-conditions) on Wiley Online Library for rules of use; OA articles are governed by the applicable Creative Commons License